coatings

MDPI

Article

Effect of Annealing Temperature on the Structure and Properties of La_2O_3 High-K Gate Dielectric Films Prepared by the Sol-Gel Method

Zhenchuan Lu [1,2], Kamale Tuokedaerhan [1,2,*], Haotian Cai [1,2], Hongguo Du [1,2] and Renjia Zhang [1,2]

[1] Xinjiang Key Laboratory of Solid State Physics and Devices, Xinjiang University, Urumqi 830046, China
[2] School of Physics Science and Technology, Xinjiang University, Urumqi 830046, China
* Correspondence: kamale9025@163.com

Abstract: This article presents the sol-gel method for depositing La_2O_3 thin films on n-type Si substrates and quartz substrates, and investigates the impact of annealing temperature on the microcomposition, surface morphology, optical properties, and band characteristics of the films. X-ray diffraction (XRD) analysis indicates that the films are amorphous below 500 °C, with annealing resulting in a hexagonal-phase La_2O_3 (h-a_2O_3) and new non-hydrated impurities. Fourier-transform infrared (FTIR) analysis reveals that the prepared La_2O_3 film is unaffected by moisture. Atomic force microscopy (AFM) and scanning electron microscopy (SEM) provide evidence that the La_2O_3 film has a smooth, uniform surface without cracks. The roughness increases from 0.426 nm to 1.200 nm, and the film thins from 54.85 nm to 49.80 nm as the annealing temperature rises. The film's transmittance is above 75%, as measured by UV-Vis, and the calculated optical bandgap increases from 5.11 eV to 5.75 eV. The calculated band offset of the La_2O_3 film is greater than 1 eV, which meets the minimum requirements for MOS devices, thus providing promising prospects for La_2O_3 films in MOS applications.

Keywords: high k gate dielectric; sol-gel; La_2O_3; thin film

check for updates

Citation: Lu, Z.; Tuokedaerhan, K.; Cai, H.; Du, H.; Zhang, R. Effect of Annealing Temperature on the Structure and Properties of La_2O_3 High-K Gate Dielectric Films Prepared by the Sol-Gel Method. *Coatings* **2023**, *13*, 1085. https://doi.org/10.3390/coatings13061085

Academic Editor: Sandra Dirè

Received: 8 April 2023
Revised: 4 June 2023
Accepted: 6 June 2023
Published: 12 June 2023

Copyright: © 2023 by the authors. Licensee MDPI, Basel, Switzerland. This article is an open access article distributed under the terms and conditions of the Creative Commons Attribution (CC BY) license (https://creativecommons.org/licenses/by/4.0/).

1. Introduction

The microelectronics industry is still predominantly using the "scaling down" technique of silicon-based complementary metal-oxide-semiconductor (CMOS) devices to achieve miniaturization, low power consumption, and high reliability [1–5]. However, as the devices become smaller, the leakage-current- and power-consumption-related issues caused by the physical limit of the conventional gate oxide SiO_2 result in the failure of semiconductor devices [6]. Therefore, researchers have chosen high-k materials to replace SiO_2 as the gate material of CMOS devices to address the issues of the charge tunneling effect brought about by the development of the technology [7–9]. In addition to needing high k values, high-k materials used as gate dielectrics in CMOS devices need to meet the following requirements: (1) moderate bandgap width (E_g), conduction band offset (ΔE_c), and valence band offset (ΔE_v) [10]; (2) the high-k gate dielectric thin film should have a single crystal or amorphous morphology [11,12]; (3) good thermal stability between the substrate and the high-k dielectric material [13]. Among them, silicon oxynitride (SiO_xN_y) is one of the earliest high-k gate dielectric materials that have been studied. However, in the 2007 ITRS report, it could no longer meet the requirements of gate leakage for continued miniaturization [14]. Subsequently, materials such as HfO_2, TiO_2, ZrO_2, and rare earth oxides have been widely used as high-k gate dielectric materials [15,16].

Rare earth elements, represented by La_2O_3, have high dielectric constant (~27), wide bandgap (~5.3 eV), and significant conduction band offset with Si substrate, as well as good thermal stability, making it one of the most promising alternative materials in CMOS devices [17,18]. The high-k value and large bandgap of La_2O_3 result in relatively low

leakage current in its application in CMOS devices. Wu et al. [19] applied a variety of high-k materials to ideal MOS devices and conducted quantum mechanical simulation experiments based on the WKB approximation. The results showed that the direct tunneling current decreases with the increase in dielectric constant or barrier height, with La_2O_3 having the lowest leakage current. La_2O_3 also possesses excellent properties in terms of electrical characteristics. Kakushima et al. [20] prepared La_2O_3 thin films and tested the electrical characteristics of sample MOSFETs. It was shown that the peak mobility increased from 60 cm^2/Vs to 300 cm^2/Vs and the subthreshold swing (SS) decreased from 120 mV/dec to 66 mV/dec. La_2O_3 exists in the cubic phase (c-La_2O_3) at low temperatures, while at high temperatures it exists mainly in the hexagonal phase (h-La_2O_3) [21,22]. h-La_2O_3 is commonly used as a gate dielectric in metal oxide semiconductor field effect transistors (MOSFETs) [23–25].

There are several methods for preparing films, including ion beam sputtering [26], chemical vapor deposition [27], and atomic layer deposition [28]. Although these technologies can produce films with excellent structures and properties, most of them require high-vacuum conditions and complex operations, resulting in high production costs. In comparison, the sol-gel method [29,30], which is inexpensive and easy to operate, is our preferred technology for preparing large-area, high-purity, and uniform thin films. Using the sol-gel method, sub-nanometer smooth $La_xZr_yO_z$ (LZO) films have been successfully prepared and have exhibited excellent electrical properties [31]. However, in previous reports, the dielectric constant of La_2O_3 was found to be significantly lower than its theoretical value of 27, and even lower than 10 [32,33]. Researchers have found that one important reason for this is the strong hygroscopicity of La_2O_3, which is unstable and forms $La(OH)_3$ or LaOOH in atmospheric environment, leading to a decrease in its dielectric constant. The hygroscopicity of La_2O_3 is due to its high ionization, which causes a direct reaction with H_2O:

$$La_2O_3 \rightarrow 2La^{3+} + 3O^{2-} \quad (1)$$

$$H_2O + O^{2-} \rightarrow 2OH^- \quad (2)$$

Experimental results showed that after being exposed to air for 12 h, the root mean square (RMS) surface roughness of La_2O_3 increased from 0.5 nm to 2.4 nm, which may be due to uneven volume expansion caused by moisture absorption of the La_2O_3 film [34]. Therefore, in this study, La_2O_3 thin films with excellent surface morphology were obtained by annealing in a nitrogen atmosphere and storing them in a vacuum environment. The sol-gel method, which is currently not extensively studied, was used to prepare La_2O_3 thin films to systematically investigate the microstructure, surface morphology, optical properties, and band characteristics of La_2O_3 thin films at different annealing temperatures. The feasibility of La_2O_3 thin films prepared by the sol-gel method as gate dielectric thin films in CMOS devices was evaluated.

2. Materials and Methods

2.1. Precursor Solution Preparation

The preparation of the precursor solution involves two processes: hydrolysis of lanthanum nitrate hexahydrate ($La(NO_3)_3 \cdot 6H_2O$, Aladdin, Shanghai, China 99.5%) and aging of $La(NO_3)_3 \cdot 6H_2O$. Firstly, $La(NO_3)_3 \cdot 6H_2O$ was dissolved in ethylene glycol monomethyl ether ($C_3H_8O_2$, Aladdin, Shanghai, China) to prepare a precursor solution with a concentration of 0.3 mol/L. Secondly, the solution was sonicated for 10 min and stirred for an hour in a stirrer. A solution of citric acid ($C_6H_8O_7$, Sinopharm Chemical Reagent Co., Ltd., Shanghai, China), with a molar ratio of 1:1 to $La(NO_3)_3 \cdot 6H_2O$ metal, was dissolved into 10 mL of $C_3H_8O_2$ and stirred for 1 h on a magnetic stirrer. The citric acid solution was slowly added dropwise to the stirring $La(NO_3)_3 \cdot 6H_2O$ solution and stirred for 2 h. Finally, 250 µL of deionized water was added and stirred for an additional 3 h to ensure complete hydrolysis reaction. The solution was then vacuum aged at 30 °C in a light-avoiding area for 48 h to obtain the La_2O_3 precursor solution.

2.2. Preparation of La_2O_3 Films

In this work, La_2O_3 films were prepared on n-type silicon (001) and quartz substrates with a resistivity of 0–20 Ω·cm using the sol-gel method. First, the substrates were sonicated in deionized water for 30 min, followed by sonication in acetonefor 20 min to remove organic substances and impurity ions on the surface. Next, the substrates were cleaned with ethanol to remove any acetone residue from the previous step. Then, 1% diluted hydrofluoric acid (HF, Tianjin Xinbote Chemical Co., Ltd., 40%, Tianjin, China) was used to sonicate the substrates and eliminate the naturally formed oxide layer on the surface. Finally, the substrates were sonicated in deionized water, vacuum dried, and stored for later use.

After filtering the precursor solution through a 0.2 μm polytetrafluoroethylene (PTFE) membrane filter, the solution was dropped onto a substrate fixed on a spin coater and spun at 3000 rpm for 30 s. The coated substrate was then covered with a cover glass on a heating plate (HP-1515, Wenzhou Hanbang Electronics, Zhejiang, China) and heated for 5 min at 150 °C to cure the film and remove excess organic solvent while isolating the air.

Finally, the samples were annealed in a nitrogen atmosphere at 400, 500, 600, and 700 °C for 2 h using a vacuum tube furnace (OTF-1200X, Hefei Kejing Materials Technology Co., Ltd., Hefei, China). The annealing rate was set at 10 °C/min, and after annealing, the furnace was cooled to room temperature.

2.3. Film Characterization

The microstructure of La_2O_3 thin film was analyzed by X-ray diffraction (XRD) using Cu Kα radiation with a scanning rate of 3°/min and a scanning range of $20° \leq 2\theta \leq 60°$, performed with a Bruker instrument located in Karlsruhe, Germany; Fourier transform infrared spectroscopy (FTIR, Bruker, Karlsruhe, Germany); and steady-state and time-resolved fluorescence spectrometer (FLS1000/FS5, Edinburgh Instruments, Edinburgh, UK). Atomic force microscopy (AFM, Bruker Dimension Fastscan) and scanning electron microscopy (SEM, HELIOS Nano Lab 600i) were used to describe the morphology of the film. X-ray photoelectron spectroscopy (XPS, Thermo Fisher ESCALAB 250Xi) was used to determine the chemical bonding and valence band spectra of the film. Ultraviolet-visible spectrophotometry (UV-Vis, Lambda 650S, PerkinElmer, Norwalk, CT, USA) was used to measure the transmission spectra of the film deposited on a quartz substrate and to calculate the band gap.

3. Results

3.1. Microstructure Analysis

Figure 1 shows X-ray diffraction (XRD) patterns of La_2O_3 films deposited on the Si substrate at different annealing temperatures. The standard XRD pattern from the Powder Diffraction File (PDF-05-0602) of the Joint Committee on Powder Diffraction Standards (JCPDS) was added to compare with the sample XRD patterns and confirm the crystalline phase of the La_2O_3 film as h-La_2O_3. La_2O_3 has a hygroscopic property and tends to hydrate with water from the air. Therefore, thermal annealing for La_2O_3 film preparation was conducted in a vacuum environment and immediately followed by vacuum storage to avoid exposure to moisture. As a result, no diffraction peaks of h-$La(OH)_3$ or LaOOH were observed in the La_2O_3 film, indicating that the film was not affected by water vapor in the air during preparation and storage.

Thin films at 400 °C and 500 °C did not show any diffraction peaks, indicating that the films were in an amorphous state below 500 °C. As the temperature increased, weak diffraction peaks appeared in the film at 600 °C, located at $2\theta = 29.96°$ and 39.53°, corresponding to the (101) and (102) crystal planes of standard h-La_2O_3 [35,36]. Similarly, in the diffraction peaks observed at 700 °C, characteristic diffraction peaks were observed at the same positions, and the crystallinity significantly increased. The results indicate that the crystalline state of the film did not undergo obvious changes with the increase in annealing temperature and no phase transition occurred, demonstrating good thermal stability. The

inset in Figure 1 shows the photoluminescence (PL) spectrum of a crystallized thin film under 365 nm ultraviolet light irradiation. The curve in the figure is smooth, and no peak representing defects is observed. Moreover, with the increase of annealing temperature, no significant change can be seen in the PL spectrum, indicating that the structural changes are not caused by defects.

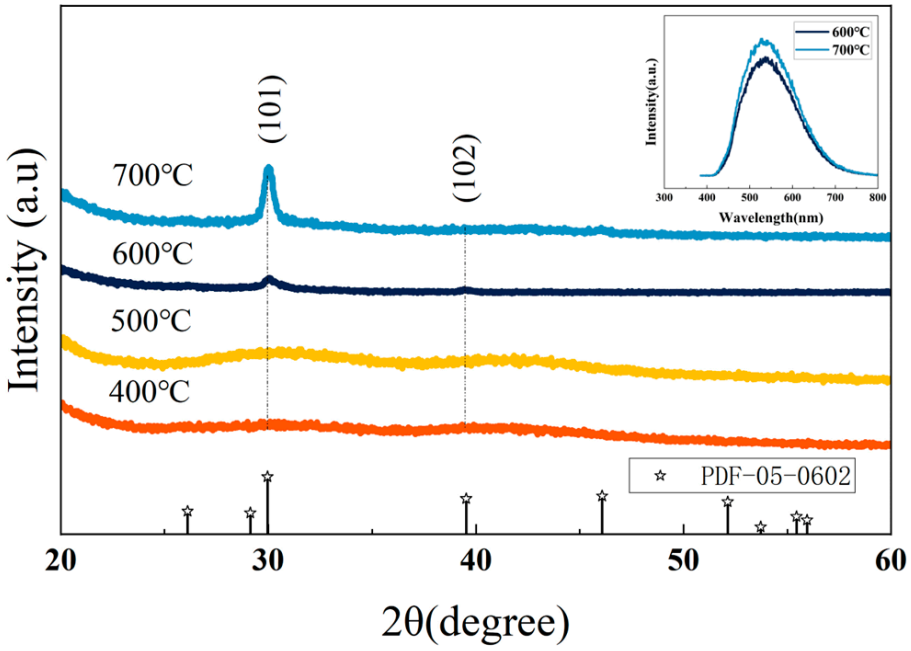


Figure 1. The X-ray diffraction (XRD) patterns of La_2O_3 thin films annealed at temperatures of 400–700 °C. The inset shows photoluminescence (PL) spectra of La_2O_3 films annealed at 600 °C and 700 °C.

The FTIR spectroscopy is employed to detect the levels of hydroxides, water, and nitrates in La_2O_3 thin film after annealing at different temperatures. According to research, the remaining hydroxides and water are monitored by the broad O-H stretching mode peak near 3500 cm^{-1} and the sharp H-O-H bending mode peak near 1650 cm^{-1}, respectively [31,37,38]. Figure 2 displays the FTIR spectra of La_2O_3 thin films annealed at different temperatures. It can be observed that there are no peaks appearing near 3500 cm^{-1} and 1650 cm^{-1} as mentioned above, and the curves are smooth, indicating that the vacuum environment was well maintained during the preparation process, and the thin film samples had either no adsorbed water or only a small amount present, and had undergone complete condensation. The content of NO_x (monitored via the N-O stretching mode with a center around 1280 cm^{-1} and 1460 cm^{-1}) [31] decreased sharply at 600 °C and 700 °C. The NOx mainly originated from $La(NO_3)_3 \cdot 6H_2O$. Similarly, the absorption band at 1465 cm^{-1} corresponded to the carbonates produced by the reaction of CO_2 and water vapor in the atmosphere with the La_2O_3 surface. Due to the alkaline properties of La_2O_3, the carbonates were formed and chemically adsorbed on its surface [39,40]. As the temperature increased, there was a significant decrease in peak intensity within this wavenumber range. These losses are crucial for the stability of the film, but at temperatures as high as 700 °C, residual NO_x seems to still be retained in the film. The peak appearing at 750 cm^{-1} corresponds to the vibrational mode of O-La-O [41,42].

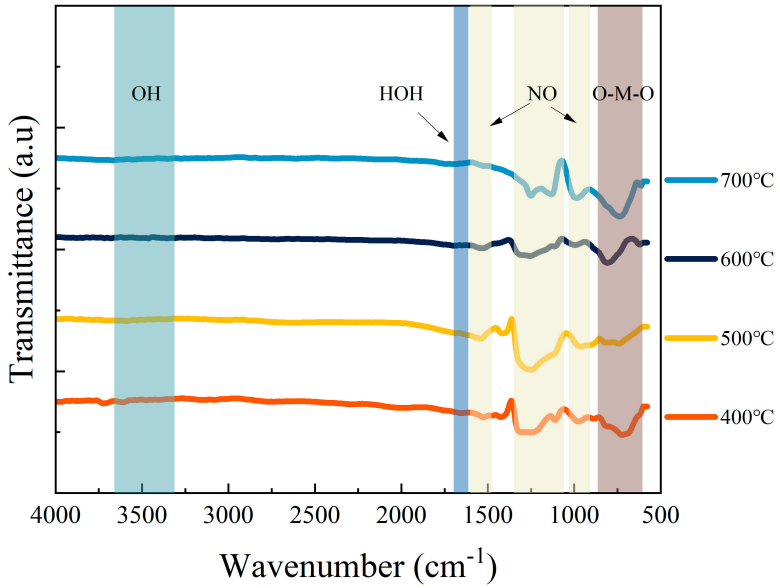


Figure 2. FTIR spectra of La_2O_3 thin films annealed at temperatures of 400–700 °C.

3.2. Micromorphology Surface Morphology

Scanning electron microscopy (SEM) was performed to analyze the surface and cross-section of the thin film samples for morphological analysis. Figure 3 shows the SEM images of the surface and cross-section of La_2O_3 films annealed at different temperatures. It can be observed from the images that all La_2O_3 films are uniform, dense, and continuously intact. However, at an annealing temperature of 700 °C (Figure 3d), irregular bright grains appeared on the surface of the film, with clear particle boundaries, leading to an increase in surface roughness. The inserted figure shows the cross-sectional SEM image of the sample, and it can be clearly seen that the thickness of the film decreased from the initial 54.85 nm to 49.80 nm. This may be due to the transformation of hydroxy groups in the film prepared by sol-gel method into oxides, as well as the volatilization of residual solvents in the film. In addition, there is no gap between the film and the substrate bonding, which is tight and seamless.

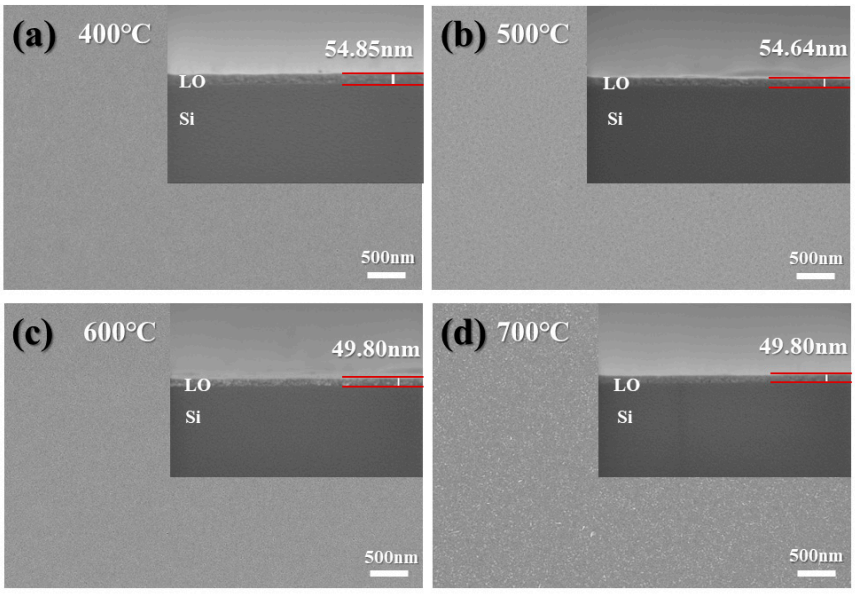


Figure 3. SEM images of La_2O_3 thin films at different annealing temperatures. (**a**–**d**) at 400, 500, 600, 700 °C annealing respectively. The inset shows SEM patterns of La_2O_3 films cross-sections annealed at 400–700 °C.

Figure 4a–d gives the surface microstructure maps of the tested thin film samples at different annealing temperatures. AFM tests were performed for the samples at annealing temperatures of 400 °C, 500 °C, 600 °C, and 700 °C with a scan range of 1 μm × 1 μm. Three AFM tests were conducted on the same sample, and the corresponding RMS roughness standard deviations were found to be 0.403 ± 0.064 nm, 1.059 ± 0.096 nm, 1.201 ± 0.255 nm, and 1.240 ± 0.115 nm. The La_2O_3 films have a relatively rough surface and the surface roughness varies with large amplitude and high span, exhibiting a surface nearly twice as rough as 400 °C, at 500 °C, presumably due to the change in crystal shape. Through the XRD analysis, we found that the film was in the process of amorphous to crystalline transition at 500 °C. It was clearly observed that the film started to crystallize at 600 °C and the crystallinity increased with increasing temperature; therefore, it was speculated that the crystallization characteristics of the film led to the change in roughness. The increase in temperature also makes the molecules and atoms of the object more active, and after obtaining enough energy, the atomic clusters merge further, prompting the clustering of small molecules into large molecular clusters. The crystallization also produces the result of large grains [43].

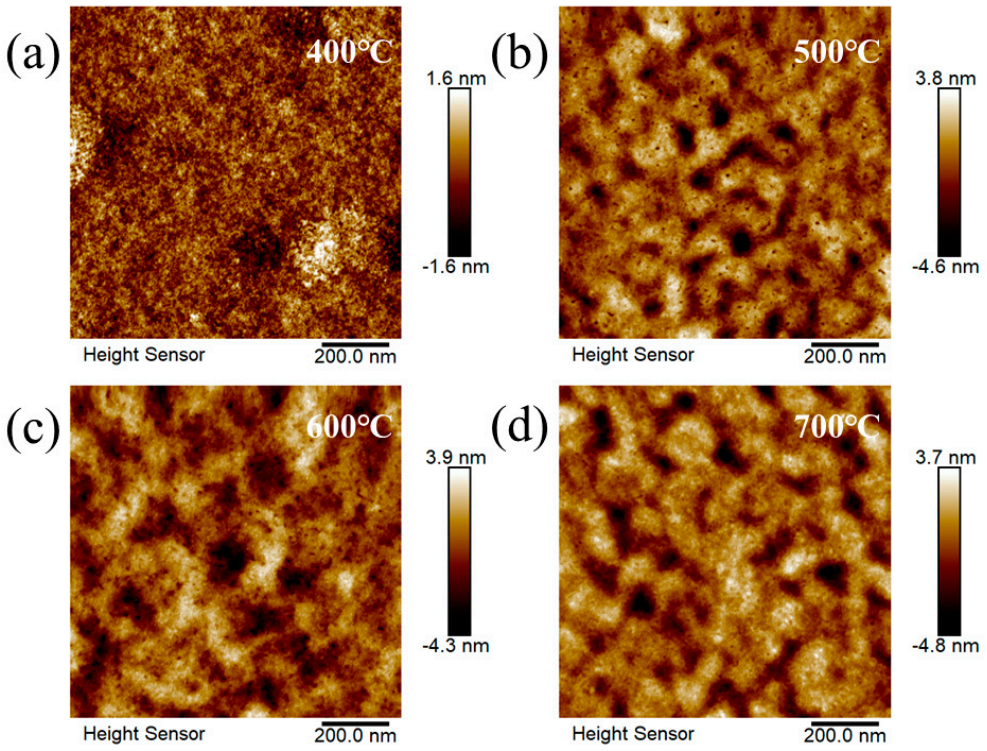


Figure 4. AFM images of La_2O_3 thin film at different annealing temperatures. (**a**–**d**) at 400, 500, 600, 700 °C annealing respectively.

3.3. Chemical Bonding Analysis

XPS analysis was employed to analyze the composition of La_2O_3 thin films deposited on silicon substrate at different annealing temperatures. Figure 5a shows the XPS full spectra of the La_2O_3 films at 400 °C–700 °C. It is evident from the full spectra that the samples contain elements such as lanthanum, oxygen, and silicon.

In Figure 5b, the La 3d spectrum of the La_2O_3 films at different temperatures can be seen. The La 3d spectrum has a main peak (La $3d_{5/2}$) and a spin-splitting peak (La $3d_{3/2}$), with their differences being 16.70 eV, 16.85 eV, 16.90 eV, and 17.00 eV at 400–700 °C, respectively. According to literature, the splitting energy of La $3d_{3/2}$ and La $3d_{5/2}$ is about 16.80 eV, representing the La+ state, and the binding energy range of La $3d_{5/2}$ (La^{3+}) in La_2O_3 is 834.0–835.1 eV [21]. The shift towards a lower binding energy indicates the presence of O–O bonding in the middle of the La_2O_3 film layer. As the temperature

increases to 700 °C, the binding energy shifts towards a higher energy range, which can be explained by the second-nearest-neighbor effect, due to the La-silicate layer being closer to the interface of the Si substrate [44].

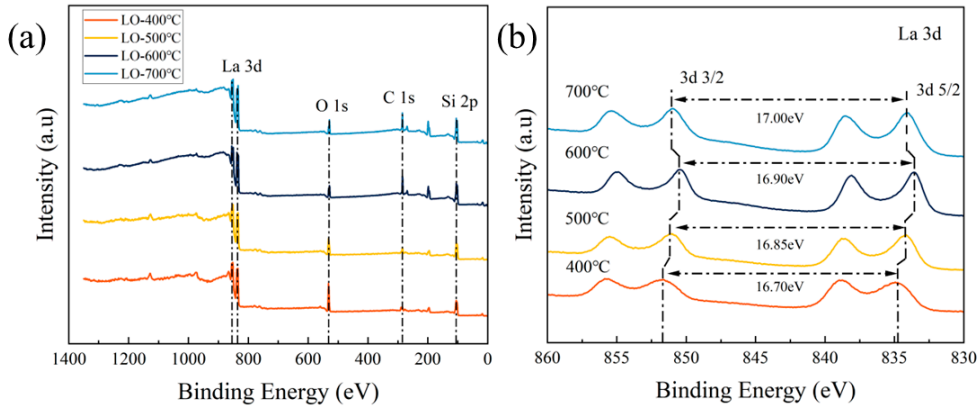


Figure 5. (**a**) XPS full spectrum of La_2O_3 films at annealing temperature of 400–700 °C, (**b**) La 3d spectrogram.

Figure 6 shows the O 1s XPS spectra of La_2O_3 thin films annealed at temperatures ranging from 400 °C to 700 °C. By fitting the O 1s spectra of the thin film samples, it was found that the film could be divided into lattice oxygen (La-O), oxygen vacancies (Vo), and hydroxyl groups (La-OH) covalently bonded with La ions at the annealing temperatures of 400 °C to 700 °C. The existence of La-OH was due to the incomplete evaporation of the sol-gel precursor [22]. It was observed that the contents of La-OH and Vo were high at 400 °C, and gradually decreased with increasing temperature, while the content of La-O increased significantly. This can be explained by the thermal-driven condensation of La-OH bonds into La-O bonds at higher temperatures, and the suppression of oxygen vacancies (Vo) generation by the annealing temperature, which increased the coordination number of metal ions and promoted the bonding between metal and oxygen ions [21].

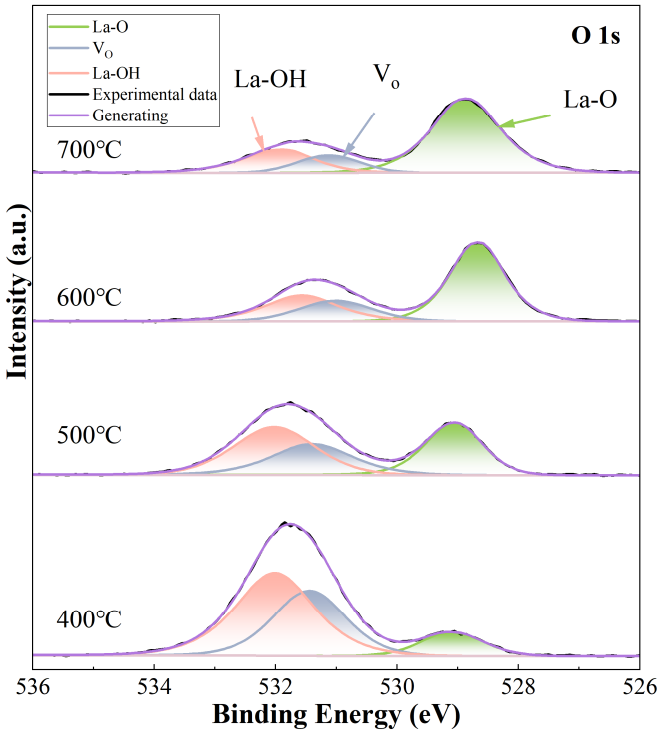


Figure 6. O 1s spectra of La_2O_3 films at annealing temperature of 400–700 °C.

3.4. Optical Properties

La_2O_3 thin films were prepared on quartz substrates at different annealing temperatures, and their optical properties were characterized using UV-Vis spectrophotometry in the wavelength range of 200–800 nm. Figure 7 shows that La_2O_3 thin films on quartz substrates exhibit high transmittance within the range of 200–800 nm, and the average transmittance of all the thin film samples is above 75%. The change in transmittance is caused by the alteration of the thin film crystal structure and thickness due to annealing temperature. Analysis of the XRD spectra shows that the thin film sample at 500 °C is in a mixed state of crystalline and amorphous phases with many defects. Therefore, the scattering of the thin film is strong, resulting in a lower transmittance at the temperature than that at 400 °C [21]. When the annealing temperature was set at 600 °C and 700 °C, the film thickness decreased to 49.80 nm, resulting in a higher transmittance of the thin film sample than that of the sample annealed below 500 °C. However, with the increase of crystallinity, the sample annealed at 700 °C had more interfacial scattering due to the increase of crystal planes, resulting in a lower transmittance compared to the sample annealed at 600 °C.

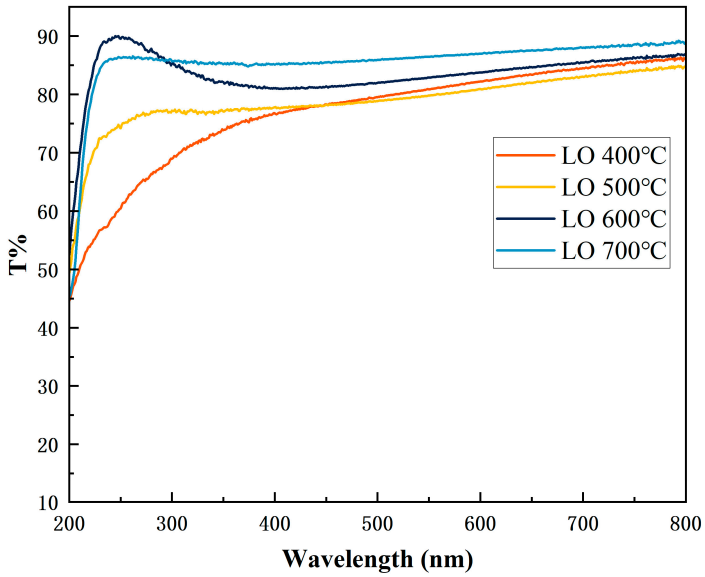


Figure 7. UV-Vis spectra of La_2O_3 films at annealing temperature of 400–700 °C.

3.5. Energy Level Characterization

In this experiment, the transmittance of the La_2O_3 thin film deposited on a quartz substrate was measured in the UV range. Using the Tauc formula, the relationship between $(\alpha h\upsilon)^2$ and $h\upsilon$ was obtained, and the bandgap width was calculated [45,46]:

$$(\alpha h\upsilon)^2 = A(h\upsilon - E_g) \quad (3)$$

where α, $h\upsilon$, A, and Eg are the absorption coefficient, photon energy, constant, and optical band gap of the La_2O_3 film, respectively. Figure 8a–d show the curves of $(\alpha h\upsilon)^2$ versus $h\upsilon$ for the films deposited on the quartz substrate. The bandgap values are obtained by tangenting the curves related to $h\upsilon$ and $(\alpha h\upsilon)^2$ for the horizontal and vertical axes, respectively. Figure 8 shows the relationship between the optical bandgap and annealing temperature. The results indicate that the bandgap of La_2O_3 film increases from 5.31 eV to 5.74 eV as the annealing temperature increases up to 600 °C [46]. However, as the temperature is further increased from 600 °C to 700 °C, the bandgap width of the La_2O_3 film starts to decrease, dropping from 5.74 eV to 5.73 eV. This may be due to the transition of the film from a short-range ordered, long-range disordered state to a long-range ordered state with increasing temperature.

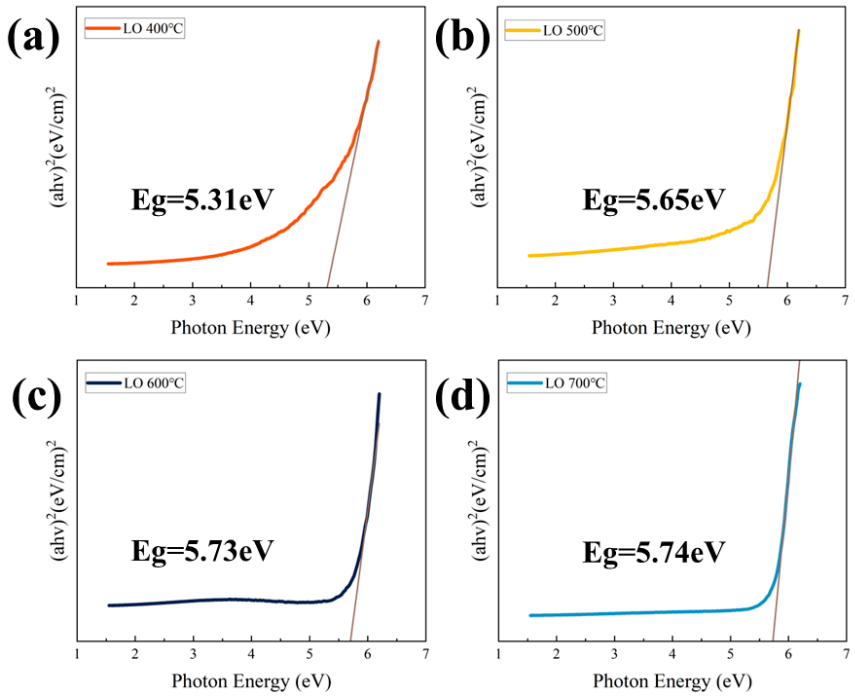


Figure 8. (**a**–**d**) Optical band gap mapping of La_2O_3 films at annealing temperature of 400–700 °C.

In this experiment, the determination of valence band discontinuity (ΔEv) and conduction band discontinuity (ΔEc) between the La_2O_3 thin film and the Si substrate was conducted using a core-level method based on the photoelectric effect. The values of ΔEv and ΔEc determined using this method can be obtained by calculating Equations (4) and (5) [47]:

$$\Delta E_v(La_2O_3/Si) = E_v(La_2O_3) - E_v(Si) \quad (4)$$

In this study, Ev(La_2O_3) refers to the highest valence band maximum (VBM) of the La_2O_3 thin film with respect to the silicon substrate, which is determined using linear extrapolation of the valence band maximum position of the La_2O_3 thin film. Figure 9a provides the valence band spectra of the La_2O_3 thin films annealed at different temperatures, with VBM values of 2.20 eV, 1.93 eV, 2.50 eV, and 2.82 eV for the thin films annealed at 400 °C, 500 °C, 600 °C, and 700 °C, respectively. Ev(Si) represents the valence band maximum of the silicon substrate, with a value of 0.50 eV. Based on the aforementioned equation, the VBO values at annealing temperatures of 400 °C, 500 °C, 600 °C, and 700 °C are determined to be 1.70 eV, 1.43 eV, 2.00 eV, and 2.32 eV.

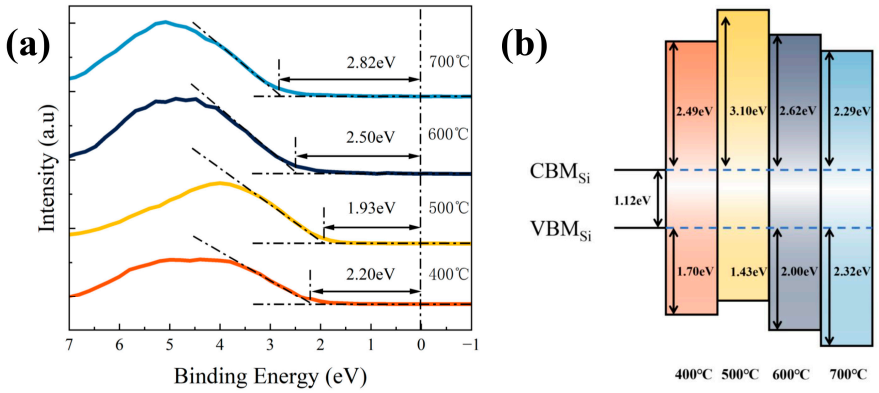


Figure 9. (**a**) Valence band spectra of La_2O_3 films at annealing temperature of 400–700 °C, (**b**) Schmatic of band gap offset.

The conduction band shift ΔEc of the La_2O_3 film can be calculated from (5) as:

$$\Delta E_c\left(La_2O_3/Si\right) = E_g(La_2O_3) - \Delta E_v\left(La_2O_3/Si\right) - E_g(Si) \quad (5)$$

In this study, Eg (La_2O_3) denotes the bandgap of the La_2O_3 thin film, which was measured using UV-Vis analysis of the film deposited on a quartz substrate, as described earlier. The bandgap value of the silicon substrate is known to be 1.12 eV. Using the relevant equation, the maximum conduction band values at annealing temperatures of 400 °C, 500 °C, 600 °C, and 700 °C are determined to be 2.49 eV, 3.10 eV, 2.62 eV, and 2.29 eV, respectively. Figure 9b illustrates the schematic energy band alignment of the La_2O_3 films on the silicon substrate at different annealing temperatures, based on the calculated and measured data. As previously reported, the band offset for gate dielectric layers should be greater than 1 eV. In this work, all La_2O_3 thin films fulfill this requirement, with a significant VBO and CBO exceeding 2 eV observed in the samples annealed above 600 °C, indicating that La_2O_3 is a promising high-k material for meeting the demand for band offset in CMOS devices, and can effectively suppress carrier tunneling phenomena.

4. Conclusions

In this study, La_2O_3 thin films were successfully prepared via the sol-gel method, and their microstructure, interfacial chemistry, optical properties, and bandgap width were systematically analyzed. The results showed that the La_2O_3 thin film started to crystallize at 600 °C and was confirmed to be h-La_2O_3 by comparison with the standard PDF card, with no impurity peaks generated. FTIR further confirmed that there was only a small amount of adsorbed water on the film surface. The film was tightly bound to the substrate, and the thickness decreased from 54.85 nm to 49.80 nm with the increase of annealing temperature, while the surface roughness showed an increasing trend. This indicates that although the increasing annealing temperature is conducive to improving the density of the film, too high a temperature may cause further atomic aggregation of the film. The La_2O_3 thin film has a high transmittance in the range of 200–800 nm, all above 70%, and the optical bandgap was calculated. The highest bandgap width of 5.74 eV was achieved at 600 °C, and both the conduction band offset and the valence band offset met the lowest requirements for CMOS barrier height.

Author Contributions: Conceptualization, methodology and validation, Z.L.; formal analysis, K.T.; investigation, Z.L.; resources and supervision, H.C., H.D. and R.Z.; data curation, writing—original draft preparation, and writing—review and editing, Z.L.; project administration and funding acquisition, K.T. All authors have read and agreed to the published version of the manuscript.

Funding: This research was supported by the Natural Science Foundation of Xinjiang Uygur Autonomous Region (Grand No. 2021D01C035), the National Natural Science Foundation of China (Grant No. 62141402), and was sponsored by Tianshan Innovation Team Program of Xinjiang Uygur Autonomous Region (Grand No. 2020D14038).

Institutional Review Board Statement: Not applicable.

Informed Consent Statement: Not applicable.

Data Availability Statement: Data are contained within the article.

Acknowledgments: This work is supported by the Key Laboratory of Solid State Physics and Device, Xinjiang University, Xinjiang, China.

Conflicts of Interest: The authors declare no conflict of interest.

References

1. Li, S.; Lin, Y.; Wu, Y.; Guo, Y.; Yu, H.; Miao, R.; Wang, Z.; Tian, W.; Li, X. Effect of Fe impurity on performance of La_2O_3 as a high k gate dielectric. *Ceram. Int.* **2019**, *45*, 21015–21022. [CrossRef]
2. Qiu, C.; Zhang, Z.; Xiao, M.; Yang, Y.; Zhong, D.; Peng, L.-M. Scaling carbon nanotube complementary transistors to 5-nm gate lengths. *Science* **2017**, *355*, 271–276. [CrossRef]

3. Zdorovets, M.V.; Kozlovskiy, A.L.; Borgekov, D.B.; Shlimas, D.I. Influence of irradiation with heavy Kr^{15+} ions on the structural, optical and strength properties of BeO ceramic. *J. Mater. Sci. Mater. Electron.* **2021**, *32*, 15375–15385. [CrossRef]
4. Trukhanov, S.V.; Troyanchuk, I.O.; Trukhanov, A.V.; Fita, I.M.; Vasil'ev, A.N.; Maignan, A.; Szymczak, H. Magnetic properties of $La_{0.70}Sr_{0.30}MnO_{2.85}$ anion-deficient manganite under hydrostatic pressure. *J. Exp. Theor. Phys. Lett.* **2006**, *83*, 33–36. [CrossRef]
5. Zhang, L.; Xing, H.; Yang, M.; Dong, Q.; Li, H.; Liu, S. Advances in atomic layer deposited high-κ inorganic materials for gate dielectrics engineering of two-dimensional MoS_2 field effect transistors. *Carbon Lett.* **2022**, *32*, 1247–1264. [CrossRef]
6. Liu, L.; Tang, W.; Lai, P. Advances in La-Based High-k Dielectrics for MOS Applications. *Coatings* **2019**, *9*, 217. [CrossRef]
7. Gao, J.; He, G.; Liu, M.; Lv, J.G.; Sun, Z.Q.; Zheng, C.Y.; Jin, P.; Xiao, D.Q.; Chen, X.S. Modulation of interfacial and electrical properties of ALD-derived $HfAlO/Al_2O_3/Si$ gate stack by annealing temperature. *J. Alloys Compd.* **2017**, *691*, 504–513. [CrossRef]
8. Kozlovskiy, A.L.; Zdorovets, M.V. Effect of doping of $Ce^{4+/3+}$ on optical, strength and shielding properties of $(0.5 - x)TeO_{2-0.25}MoO_{-0.25}Bi_2O_{3-x}CeO_2$ glasses. *Mater. Chem. Phys.* **2021**, *263*, 124444. [CrossRef]
9. Khan, S.A.; Ali, I.; Hussain, A.; Javed, H.M.A.; Turchenko, V.A.; Trukhanov, A.V.; Trukhanov, S.V. Synthesis and Characterization of Composites with Y-Hexaferrites for Electromagnetic Interference Shielding Applications. *Magnetochemistry* **2022**, *8*, 186. [CrossRef]
10. Talalaev, F.; Luchkin, S.; Mumyatov, A.V.; Zhidkov, I.S.; Lobanov, M.V.; Emelianov, N.A.; Babenko, S.D.; Kurmaev, E.Z.; Aldoshin, S.M.; Troshin, P.A. High-Performance Organic Field-Effect Transistors Using Rare Earth Metal Oxides as Dielectrics. *ACS Appl. Electron. Mater.* **2023**, *5*, 2000–2006. [CrossRef]
11. Arafune, K.; Kitano, S.; Yoshida, H.; Ogura, A.; Hotta, Y. Effect of post-deposition annealing on electrical properties and structures of aluminum oxide passivation film on a crystalline silicon substrate. *Jpn. J. Appl. Phys.* **2019**, *58*, 125502. [CrossRef]
12. Hoex, B.; Schmidt, J.; Pohl, P.; van de Sanden, M.C.M.; Kessels, W.M.M. Silicon surface passivation by atomic layer deposited Al_2O_3. *J. Appl. Phys.* **2008**, *104*, 044903. [CrossRef]
13. Asad, S.u.; Rehman, S.U.; Tariq, H.; Perveen, S.; Amin, F.; Nadeem, M.; Azad, F. Effect of annealing environment on dielectric properties of erbium oxide. *Ceram. Int.* **2022**, *48*, 23536–23542. [CrossRef]
14. Krisch, K.S.; Sodini, C.G. Suppression of interface-state generation in reoxidized nitrided oxide gate dielectrics. *J. Appl. Phys.* **1994**, *76*, 2284–2292. [CrossRef]
15. Mansilla, Y.; Arce, M.D.; González-Oliver, C.; Basbus, J.; Troiani, H.; Serquis, A. Characterization of stabilized ZrO_2 thin films obtained by sol-gel method. *Appl. Surf. Sci.* **2021**, *569*, 150787. [CrossRef]
16. Lin, Y.-W.; Sun, C.-J.; Chang, H.-H.; Huang, Y.-H.; Yu, T.-Y.; Wu, Y.-C.; Hou, F.-J. Self-induced ferroelectric 2-nm-thick Ge-doped HfO_2 thin film applied to Ge nanowire ferroelectric gate-all-around field-effect transistor. *Appl. Phys. Lett.* **2020**, *117*, 262109. [CrossRef]
17. Fang, Y.; Zhao, C.; Mitrovic, I.Z.; Zhao, C. High-Performance and Radiation-Hardened Solution-Processed ZrLaO Gate Dielectrics for Large-Area Applications. *ACS Appl. Mater. Interfaces* **2021**, *13*, 50101–50110. [CrossRef]
18. Wu, Y.H.; Yang, M.Y.; Chin, A.; Member, S. Electrical Characteristics of High Quality LaPOQ Gate Dielectric with Equivalent Oxide Thickness of 5 Å. *IEEE Electron Device Lett.* **2000**, *21*, 341–343. [CrossRef]
19. Wu, H.; Zhao, Y.; White, M.H. Quantum mechanical modeling of MOSFET gate leakage for high-k gate dielectrics. *Solid-State Electron.* **2006**, *50*, 1164–1169. [CrossRef]
20. Kakushima, K.; Tachi, K.; Adachi, M.; Okamoto, K.; Sato, S.; Song, J.; Kawanago, T.; Ahmet, P.; Tsutsui, K.; Sugii, N.; et al. Interface and electrical properties of La-silicate for direct contact of high-k with silicon. *Solid-State Electron.* **2010**, *54*, 715–719. [CrossRef]
21. Yadav, A.A.; Lokhande, A.C.; Pujari, R.B.; Kim, J.H.; Lokhande, C.D. The synthesis of multifunctional porous honey comb-like La_2O_3 thin film for supercapacitor and gas sensor applications. *J. Colloid Interface Sci.* **2016**, *484*, 51–59. [CrossRef] [PubMed]
22. Gao, G.; Yang, L.; Dai, B.; Xia, F.; Yang, Z.; Guo, S.; Wang, P.; Geng, F.; Han, J.; Zhu, J. Investigation of the effect of annealing temperature on optical properties of lanthanum-oxide thin films prepared by sol-gel method. *Surf. Coat. Technol.* **2019**, *365*, 164–172. [CrossRef]
23. Fang, M.; Kelty, S.P.; He, X. Molecular dynamics simulations of La_2O_3 thin films on SiO_2. *J. Energy Chem.* **2014**, *23*, 282–286. [CrossRef]
24. Ji, H.-I.; Hwang, J.; Yoon, K.J.; Son, J.-W.; Kim, B.-K.; Lee, H.-W.; Lee, J.-H. Enhanced oxygen diffusion in epitaxial lanthanum–strontium–cobaltite thin film cathodes for micro solid oxidefuel cells. *Energy Environ. Sci.* **2013**, *6*, 116–120. [CrossRef]
25. Ohmi, S.; Kobayashi, C.; Kashiwagi, I.; Ohshima, C.; Ishiwara, H.; Iwai, H. Characterization of La_2O_3 and Yb_2O_3 Thin Films for High-k Gate Insulator Application. *J. Electrochem. Soc.* **2003**, *150*, F134. [CrossRef]
26. Sharko, S.A.; Serokurova, A.I.; Novitskii, N.N.; Ketsko, V.A.; Smirnova, M.N.; Almuqrin, A.H.; Sayyed, M.I.; Trukhanov, S.V.; Trukhanov, A.V. A New Approach to the Formation of Nanosized Gold and Beryllium Films by Ion-Beam Sputtering Deposition. *Nanomaterials* **2022**, *12*, 470. [CrossRef] [PubMed]
27. Gopalan, S.; Ramesh, S.; Dutta, S.; Garbhapu, V.V. Effects of substrate heating and post-deposition annealing on characteristics of thin MOCVD HfO_2 films. In *IOP Conference Series: Materials Science and Engineering*; IOP Publishing: Bristol, UK, 2018.
28. Park, B.-E.; Lee, Y.; Oh, I.-K.; Noh, W.; Gatineau, S.; Kim, H. Structural and electrical properties of Ge-doped ZrO_2 thin films grown by atomic layer deposition for high-k dielectrics. *J. Mater. Sci.* **2018**, *53*, 15237–15245. [CrossRef]
29. Tan, W.K.; Muto, H.; Kawamura, G.; Lockman, Z.; Matsuda, A. Nanomaterial Fabrication through the Modification of Sol-Gel Derived Coatings. *Nanomaterials* **2021**, *11*, 181. [CrossRef]

30. Tuleushev, A.Z.; Harrison, F.E.; Kozlovskiy, A.L.; Zdorovets, M.V. Evolution of the absorption edge of PET films irradiated with Kr ions after thermal annealing and ageing. *Opt. Mater.* **2021**, *119*, 111348. [CrossRef]
31. Woods, K.N.; Chiang, T.-H.; Plassmeyer, P.N.; Kast, M.G.; Lygo, A.C.; Grealish, A.K.; Boettcher, S.W.; Page, C.J. High-κ Lanthanum Zirconium Oxide Thin Film Dielectrics from Aqueous Solution Precursors. *ACS Appl. Mater. Interfaces* **2017**, *9*, 10897–10903. [CrossRef]
32. Jun, J.H.; Choi, D.J.; Kim, K.H.; Oh, K.Y.; Hwang, C.J. Effect of Structural Properties on Electrical Properties of Lanthanum Oxide Thin Film as a Gate Dielectric. *Jpn. J. Appl. Phys.* **2003**, *42*, 3519–3522. [CrossRef]
33. Yamada, H.; Shimizu, T.; Kurokawa, A. MOCVD of High-Dielectric-Constant Lanthanum Oxide Thin Films. *J. Electrochem. Soc.* **2003**, *150*, G429. [CrossRef]
34. Zhao, Y. Design of Higher-k and More Stable Rare Earth Oxides as Gate Dielectrics for Advanced CMOS Devices. *Materials* **2012**, *5*, 1413–1438. [CrossRef]
35. Hu, C.G.; Liu, H.; Dong, W.T.; Zhang, Y.Y.; Bao, G.; Lao, C.S.; Wang, Z.L. $La(OH)_3$ and La_2O_3 Nanobelts—Synthesis and Physical Properties. *Adv. Mater.* **2007**, *19*, 470–474. [CrossRef]
36. Aghazadeh, M.; Arhami, B.; Malek Barmi, A.-A.; Hosseinifard, M.; Gharailou, D.; Fathollahi, F. $La(OH)_3$ and La_2O_3 nanospindles prepared by template-free direct electrodeposition followed by heat-treatment. *Mater. Lett.* **2014**, *115*, 68–71. [CrossRef]
37. Shen, Z.; Zhao, Y.; Tian, Z.; Huang, W.; Wu, J.; Lin, H. Effect of doping La_2O_3 on the structure and properties of the titanium barium silicate glass. *J. Non-Cryst. Solids* **2018**, *499*, 17–24. [CrossRef]
38. Al-Abadleh, H.; Grassian, V.H. FT-IR Study of Water Adsorption on Aluminum Oxide Surfaces. *Langmuir* **2003**, *19*, 341–347. [CrossRef]
39. Gangwar, B.P.; Palakollu, V.; Singh, A.; Kanvah, S.; Sharma, S. Combustion synthesized La_2O_3 and $La(OH)_3$: Recyclable catalytic activity towards Knoevenagel and Hantzsch reactions. *RSC Adv.* **2014**, *4*, 55407–55416. [CrossRef]
40. Levan, T.; Che, M.; Tatibouet, J.M.; Kermarec, M. Infrared Study of the Formation and Stability of $La_2O_2CO_3$ During the Oxidative Coupling of Methane on La_2O_3. *J. Catallysis* **1993**, *142*, 18–26. [CrossRef]
41. Hussain, S.K.; Nagaraju, G.; Pavitra, E.; Seeta Rama Raju, G.; Yu, J.S. $La(OH)_3$:Eu^{3+} and La_2O_3:Eu^{3+} nanorod bundles: Growth mechanism and luminescence properties. *CrystEngComm* **2015**, *17*, 9431–9442. [CrossRef]
42. Xu, D.; Fan, D.; Shen, W. Catalyst-free direct vapor-phase growth of $Zn_{1-x}Cu_xO$ micro-cross structures and their optical properties. *Nanoscale Res. Lett.* **2013**, *8*, 46. [CrossRef] [PubMed]
43. Fan, C.; Liu, A.; Meng, Y.; Guo, Z.; Liu, G.; Shan, F. Solution-Processed SrO_x-Gated Oxide Thin-Film Transistors and Inverters. *IEEE Trans. Electron Devices* **2017**, *64*, 4137–4143. [CrossRef]
44. Lee, B.; Park, T.J.; Hande, A.; Kim, M.J.; Wallace, R.M.; Kim, J.; Liu, X.; Yi, J.H.; Li, H.; Rousseau, M.; et al. Electrical properties of atomic-layer-deposited La_2O_3 films using a novel La formamidinate precursor and ozone. *Microelectron. Eng.* **2009**, *86*, 1658–1661. [CrossRef]
45. Lei, P.; Dai, B.; Zhu, J.; Chen, X.; Liu, G.; Zhu, Y.; Han, J. Controllable phase formation and physical properties of yttrium oxide films governed by substrate heating and bias voltage. *Ceram. Int.* **2015**, *41*, 8921–8930. [CrossRef]
46. Devine, R.A.B. Infrared and electrical properties of amorphous sputtered $(La_xAl_{1-x})_2O_3$ films. *J. Appl. Phys.* **2003**, *93*, 9938–9942. [CrossRef]
47. Li, W.D.; He, G.; Zheng, C.Y.; Liang, S.; Zhu, L.; Jiang, S.S. Solution-processed HfGdO gate dielectric thin films for CMOS application: Effect of annealing temperature. *J. Alloys Compd.* **2018**, *731*, 150–155. [CrossRef]

Disclaimer/Publisher's Note: The statements, opinions and data contained in all publications are solely those of the individual author(s) and contributor(s) and not of MDPI and/or the editor(s). MDPI and/or the editor(s) disclaim responsibility for any injury to people or property resulting from any ideas, methods, instructions or products referred to in the content.